Garnet–monazite rare earth element relationships in sub-solidus metapelites: a case study from Bhutan

CLARE J. WARREN[1]*, LUCY V. GREENWOOD[1], TOM W. ARGLES[1],
NICK M. W. ROBERTS[2], RANDALL R. PARRISH[2,3] &
NIGEL B. W. HARRIS[1]

[1]*School of Environment, Earth and Ecosystem Sciences, The Open University,
Walton Hall, Milton Keynes MK7 6AA, UK*

[2]*NERC Isotope Geoscience Laboratories, British Geological Survey, Kingsley
Dunham Centre, Keyworth NG12 5GG, UK*

[3]*Present address: School of Earth and Environmental Sciences, University of
Portsmouth, Portsmouth PO1 3QL, UK*

C.J.W., 0000-0003-2444-9737; T.W.A., 0000-0002-0484-4230;
N.M.W.R., 0000-0001-8272-5432; R.R.P., 0000-0001-6801-8379;
N.B.W.H., 0000-0003-1737-487X

Correspondence: clare.warren@open.ac.uk

Abstract: A key aim of modern metamorphic geochronology is to constrain precise and accurate rates and timescales of tectonic processes. One promising approach in amphibolite and granulite-facies rocks links the geochronological information recorded in zoned accessory phases such as monazite to the pressure–temperature information recorded in zoned major rock-forming minerals such as garnet. Both phases incorporate rare earth elements (REE) as they crystallize and their equilibrium partitioning behaviour potentially provides a useful way of linking time to temperature. We report REE data from sub-solidus amphibolite-facies metapelites from Bhutan, where overlapping ages, inclusion relationships and Gd/Lu ratios suggest that garnet and monazite co-crystallized. The garnet–monazite REE relationships in these samples show a steeper pattern across the heavy (H)REE than previously reported. The difference between our dataset and the previously reported data may be due to a temperature-dependence on the partition coefficients, disequilibrium in either dataset, differences in monazite chemistry or the presence or absence of a third phase that competed for the available REE during growth. We urge caution against using empirically-derived partition coefficients from natural samples as evidence for, or against, equilibrium of REE-bearing phases until monazite–garnet partitioning behaviour is better constrained.

Supplementary material: Trace element concentrations and data, detailed analytical information, field photographs, chemical maps and thin section information are available at https://doi.org/10.6084/m9.figshare.c.4044323

Monazite, a rare earth element-bearing phosphate, is a useful geochronometer in metapelitic rocks because it is a common accessory phase that incorporates U when it crystallizes and generally excludes Pb (Parrish 1990). As with many metamorphic geochronometers, the interpretation of the U–Pb age yielded by monazite can be equivocal – monazite crystallizes over a wide-range of pressure–temperature (PT) conditions and may form via many different reactions during a single metamorphic cycle. Linking the timing of crystallization of different chemical zones of a multiply-zoned monazite crystal to the PT conditions under which it crystallized is therefore critical for linking age to the stage of

metamorphism, and for determining the rates of metamorphic processes. In cases where there is limited microstructural association (such as inclusion relationships for example), chemical fingerprints may provide evidence for co-crystallization between the chronometer and thermobarometer phases.

Both garnet and monazite incorporate rare earth elements (REE) during crystallization, with garnet preferentially incorporating the middle (MREE; Sm, Eu, Gd, Dy) and heavy rare earths (HREE; Ho, Er, Tm, Yb, Lu) and monazite the light rare earths (LREE; La, Ce, Pr, Nd; Ayres & Harris 1997). REE concentrations in both during growth are controlled by availability (e.g. release of

elements from other breaking-down phases), efficiency of transport of these elements to the growing crystal, and competition for these elements by other contemporaneously-reacting phases (e.g. Wood & Blundy 1997; Skora *et al.* 2006; Konrad-Schmolke *et al.* 2008). Concentrations may also be modified after growth by diffusional re-equilibration if temperatures are high enough (e.g. Carlson 2012).

In metamorphic garnets, a decrease in HREE concentrations from core to rim is commonly attributed to Rayleigh fractionation (Otamendi *et al.* 2002) or, in more complex cases, to diffusion-limited availability (Skora *et al.* 2006). Increases or decreases in HREE concentrations from core to rim in monazite are commonly attributed to the ascribed breakdown or growth of an HREE-rich phase during continued monazite growth (Rubatto *et al.* 2001).

Recent studies have reported the REE compositions of different monazite zones as well as their U–Pb isotopic composition (e.g. Rubatto *et al.* 2006; Mottram *et al.* 2014, 2015). These data, in conjunction with inclusion relationships and the REE compositions of coexisting garnet, provide information about how monazite and garnet compete for REE during co-crystallization under different conditions. Furthermore, the partitioning relationships between these two minerals potentially allow the recognition of co-crystallization in cases where there is no direct microtextural evidence.

We have noted that the garnet–monazite partitioning relationships in a series of sub-solidus amphibolite-facies schists and gneisses from central and western Bhutan show differences to previously reported datasets. This observation has important implications for using garnet–monazite REE concentration relationships to prove or disprove equilibrium growth and therefore link monazite age to garnet growth stage. Here we document these differences and our observations that suggest the garnet and monazite grew together. We discuss the different factors that could have led to these differences.

Geological setting

The Himalaya are the surface expression of the India–Asia collision, which initiated 55–50 million years ago (Rowley 1996; Zhu *et al.* 2005). During collision, Indian continental margin sediments were buried deep beneath Asia, metamorphosed, deformed and partially melted, and are now exposed along the orogenic front marking the southern edge of the Tibetan Plateau. The metamorphic core of the orogen, exposed as a unit of amphibolite- to granulite-facies metasediments, migmatites and granites, is commonly referred to as the Greater Himalayan Sequence or GHS (e.g. Hodges 2000). The GHS is tectonically overlain by the un-metamorphosed

Tethyan Himalayan Sequence, which represents the marine sediments originally deposited in the Tethys Ocean that separated India from Asia. The GHS is tectonically underlain by the Lesser Himalayan Sequence (LHS), which represents an isotopically distinct metasedimentary unit with a lower-grade metamorphic history. The Main Central Thrust separates the GHS from the LHS.

In Bhutan, the GHS has been subdivided into two distinct metamorphic and geochronological units: a younger, structurally higher, higher-grade unit exposed in the north and an older, structurally lower, lower-grade unit exposed in the south, separated structurally by the Laya Thrust (Fig. 1), assumed to be contiguous with the Kakthang Thrust exposed in central Bhutan (Swapp & Hollister 1991; Grujic *et al.* 2011; Warren *et al.* 2011). Migmatites containing cordierite, K-feldspar, sillimanite and relict kyanite are common in the higher structural levels, whereas non-migmatitic gneisses containing staurolite, kyanite and fibrolitic sillimanite are common at lower structural levels. The peak conditions experienced by the GHS are *c.* 630°C and 8–10 kbar near the base of the unit and 750–800°C at 10–14 kbar for migmatites at high structural levels (Daniel *et al.* 2003).

Not many studies have thus far provided constraints on the timing of metamorphism in central and western southern Bhutan. Monazite cores yielding ages ≥21 Ma have been interpreted as documenting the timing of prograde metamorphism to conditions of *c.* 700°C and 8 kbar in the GHS surrounding the Paro window (Fig. 1; Tobgay *et al.* 2012). High Y concentrations in monazite rims dated between *c.* 15 and 10 Ma were interpreted as documenting decompressive breakdown and subsequent release of Y from garnet. In central southern Bhutan, numerous studies have documented the structural and metamorphic evolution in some detail (e.g. Corrie *et al.* 2012; Long *et al.* 2012; Greenwood *et al.* 2016) but have not constrained the timing of metamorphism.

Six metapelite samples from varying structural levels of the high-grade metamorphic unit, the GHS in Bhutan were chosen for this study on the basis of their mineralogy, availability of monazite and the inclusion relationships between monazite and garnet (Fig. 1).

Methods

Major element concentrations and maps

Quantitative major-element mineral chemical data and qualitative major- and trace-element X-ray maps of garnet and monazite were collected from polished and carbon-coated sections using the Open University Cameca SX100 electron microprobe.
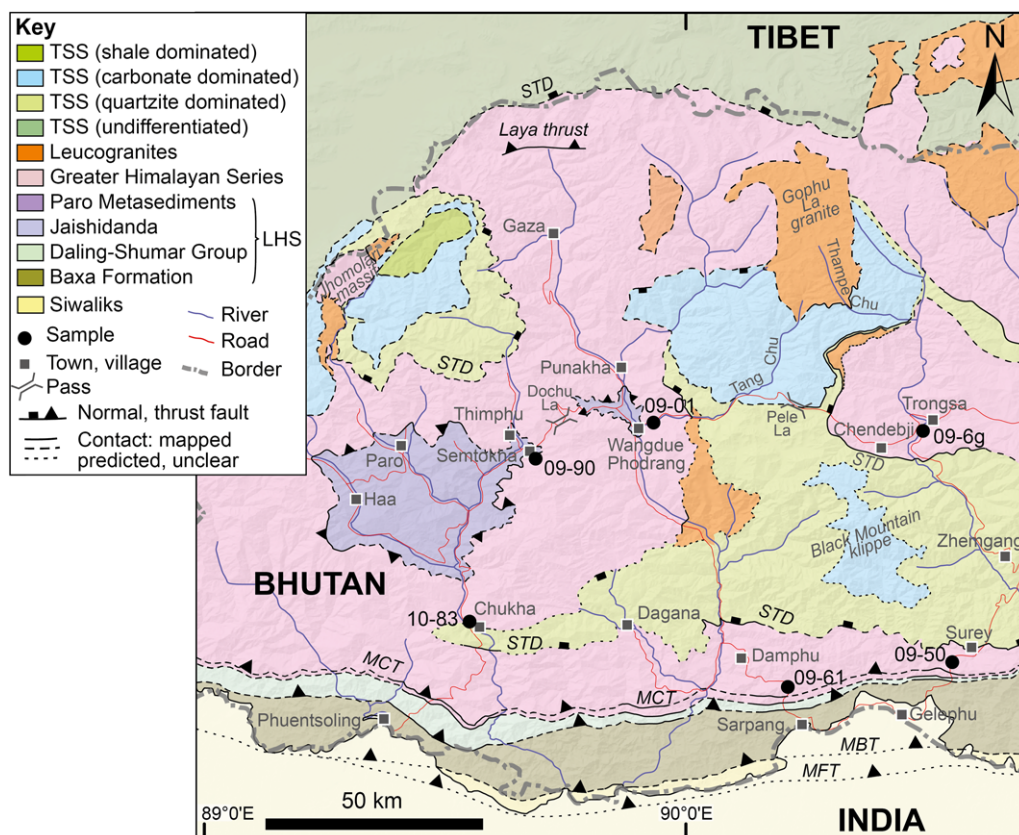
Fig. 1. Geological map of western Bhutan showing sample locations. MBT, Main Boundary Thrust; LHS, Lesser Himalayan Sequence; MCT, Main Central Thrust; MFT, Main Frontal Thrust; STD, South Tibetan Detachment; TSS, Tethyan Sedimentary Sequence; modified from Greenwood *et al.* (2016).

Operating conditions for major-element analyses involved a beam current of 20 nA, an accelerating voltage of 20 kV and data collection times of 10–30 s depending on the element. Natural standards were used for calibration, and analyses were corrected using a ZAF matrix correction routine. Sample analyses were bracketed by secondary standard analyses to check for major-element reproducibility of at least 1%.

Fe, Mg, Ca, Mn and Y concentrations in garnet were mapped at 1–10 μm resolution depending on grain size, with a 1 μm beam and 35 ms per pixel. U, Y, Th and Ce concentrations were mapped in monazite at 1 μm resolution with a 1 μm beam and collection times of 35 ms per pixel. The same operating conditions were used to generate all monazite maps and therefore relative concentrations of Ce, Th and Y are assessable between grains in the same sample and between samples. Consequently, concentrations of Ce, Th and Y in monazite are described below as 'low', 'average' and/or 'high'.

Mineral compositions provided in Table 1 and discussed in the text are an average of the compositions of 2–3 grains, with 5–15 data points collected from each grain. Where minerals are significantly zoned, compositions of the different zones are presented.

Trace element compositions

Monazite and garnet trace-element concentrations were acquired on the Open University Agilent 7500 quadrupole ICP-MS coupled to a New Wave Research UP213 (213 nm) Nd:YAG laser ablation system. The same monazites selected for U–Th–Pb dating (below) were analysed *in situ* in polished thin sections for REE concentrations. Laser spots (25–40 μm) for monazite REE analysis were sited either immediately next to, or as a larger spot engulfing the 15–20 μm pits formed during the U–Th–Pb analyses. Laser spots for garnet analysis were

Table 1. *Summary major element data for the sample rock-forming minerals*

Sample	LG-09-1						LG-09-6g								
Mineral Comment	Grt average	Bt average matrix	Mus core matrix	Mus Rim matrix	Pl average matrix	Ksp average matrix	Grt average	Pl low Ca in Grt	Pl high Ca in Grt	Pl average matrix	Bt low Fe in Grt	Bt high Fe in Grt	Bt average matrix	Mus average in Grt	Mus average matrix
SiO_2	37.05	34.68	44.62	45.51	61.88	64.19	39.44	61.32	55.82	62.30	37.73	36.50	36.09	46.34	46.99
TiO_2	0.02	2.96	0.82	0.86	0.01	0.01	0.01	0.01	0.06	0.01	1.26	1.98	1.81	0.71	0.65
Al_2O_3	20.87	18.48	33.94	34.42	24.17	18.75	20.95	23.97	28.23	23.70	18.64	18.80	18.20	33.90	34.28
FeO^T	29.77	20.47	1.65	1.96	0.02	0.02	30.81	0.16	0.65	0.01	12.83	16.97	16.71	0.98	1.16
MnO	7.64	0.28	0.01	0.02	0.01	0.00	3.07	0.02	0.06	0.00	0.04	0.09	0.08	0.01	0.02
MgO	2.73	7.78	0.57	0.52	0.00	0.00	3.63	0.00	0.00	0.00	12.75	9.55	9.69	0.77	0.80
CaO	1.73	0.06	0.02	0.04	5.37	0.07	2.04	5.32	9.67	4.63	0.05	0.01	0.02	0.01	0.00
Na_2O	0.02	9.40	10.43	10.60	0.22	14.09	0.01	8.53	5.78	8.93	0.26	0.27	0.24	1.21	1.18
K_2O	0.00	0.15	0.46	0.42	8.76	1.80	0.00	0.09	0.05	0.11	7.80	7.94	7.73	8.83	8.87
Total	99.84	94.60	92.57	94.38	100.46	98.95	99.98	99.45	100.34	99.71	91.38	92.13	90.59	93.97	92.78
Si	3.00	5.40	6.13	6.15	2.74	2.98	3.01	2.74	2.51	2.77	5.71	5.61	5.64	6.27	6.28
Ti	0.00	0.35	0.08	0.09	0.00	0.00	0.00	0.00	0.00	0.00	0.14	0.23	0.21	0.07	0.06
Al	1.99	3.39	5.54	5.48	1.26	1.03	2.07	1.26	1.49	1.24	3.32	3.41	3.35	5.40	5.40
Fe	2.01	2.67	0.19	0.22	0.00	0.00	2.09	0.01	0.02	0.00	1.62	2.18	2.18	0.11	0.13
Mn	0.52	0.04	0.00	0.00	0.00	0.00	0.20	0.00	0.00	0.00	0.01	0.01	0.01	0.00	0.00
Mg	0.33	1.81	0.11	0.10	0.00	0.00	0.42	0.00	0.00	0.00	2.88	2.19	2.26	0.16	0.16
Ca	0.15	0.01	0.01	0.01	0.25	0.00	0.17	0.25	0.47	0.22	0.01	0.00	0.00	0.00	0.00
Na	0.00	0.05	0.13	0.11	0.75	0.16	0.00	0.74	0.50	0.77	0.08	0.08	0.07	0.32	0.31
K	0.00	1.87	1.82	1.83	0.01	0.83	0.00	0.00	0.00	0.01	1.51	1.56	1.54	1.54	1.51
Total	8.01	15.70	14.04	14.01	5.02	5.01	7.96	5.00	5.00	5.00	15.27	15.27	15.28	13.86	13.88

Sample	LG-09-50					LG-09-61									
Mineral Comment	Grt average	Bt average matrix	Mus average matrix	Pl in Grt	Pl average matrix	Grt average core	Grt average outer rim	Bt high Fe in Grt	Bt low Fe in Grt	Bt average matrix	St high Fe In Grt	St low Fe in Grt	Mus in Grt	Mus average matrix	Pl average matrix
SiO_2	37.37	35.99	46.21	61.11	62.66	36.79	37.61	35.76	39.60	35.58	24.65	25.39	46.44	46.34	64.74
TiO_2	0.02	1.54	0.70	0.00	0.01	0.01	0.02	1.21	1.47	1.14	0.01	0.08	0.96	0.74	0.01
Al_2O_3	20.71	18.87	34.85	24.33	23.14	20.89	21.01	18.08	17.82	18.65	21.44	22.55	33.91	34.34	21.84
FeO^T	34.03	19.47	1.06	0.57	0.08	34.41	35.45	18.21	14.22	20.51	38.60	30.66	1.72	1.24	0.02
MnO	2.04	0.05	0.01	0.03	0.00	0.81	0.90	0.10	0.02	0.07	0.30	0.16	0.02	0.01	0.00
MgO	3.32	9.67	0.72	0.00	0.00	3.99	4.08	11.83	12.83	9.32	3.62	9.03	1.14	0.93	0.00
CaO	2.19	0.02	0.01	5.78	4.38	2.10	1.51	0.11	0.05	0.01	0.06	0.08	0.01	0.00	2.70

Na$_2$O	0.02	0.23	1.55	8.55	9.40	0.02	0.01	0.33	0.35	0.19	0.04	0.42	1.77	1.44	10.22
K$_2$O	0.00	8.27	8.85	0.06	0.08	0.06	0.00	7.94	8.05	8.73	0.05	0.03	8.57	9.00	0.08
Total	99.69	94.35	94.04	100.44	99.78	99.08	100.59	94.02	94.81	94.51	88.83	88.45	94.68	94.13	99.65
Si	3.01	5.51	6.20	2.71	2.78	2.97	3.00	5.50	5.85	5.50	4.33	4.67	6.21	6.22	2.86
Ti	0.00	0.18	0.07	0.00	0.00	0.00	0.00	0.14	0.16	0.13	0.00	0.01	0.10	0.07	0.00
Al	1.97	3.41	5.51	1.27	1.21	2.00	1.97	3.28	3.11	3.40	4.44	4.89	5.35	5.43	1.14
Fe	2.29	2.50	0.12	0.02	0.00	2.34	2.36	2.34	1.76	2.65	5.67	4.73	0.19	0.14	0.00
Mn	0.14	0.01	0.00	0.00	0.00	0.06	0.06	0.01	0.00	0.01	0.04	0.03	0.00	0.00	0.00
Mg	0.40	2.21	0.14	0.00	0.00	0.48	0.49	2.71	2.83	2.15	0.95	2.48	0.23	0.19	0.00
Ca	0.19	0.00	0.00	0.28	0.21	0.18	0.13	0.02	0.01	0.00	0.01	0.02	0.00	0.00	0.13
Na	0.00	0.07	0.40	0.74	0.81	0.00	0.00	0.10	0.10	0.06	0.02	0.15	0.46	0.37	0.88
K	0.00	1.62	1.51	0.00	0.00	0.01	0.00	1.55	1.52	1.72	0.01	0.01	1.46	1.54	0.00
Total	8.00	15.61	13.99	5.02	5.02	8.04	8.01	15.87	15.52	15.77	15.49	16.97	14.06	14.01	5.01

Sample	LG-09-90						LG-10-83						
Mineral Comment	Grt average	Bt in Grt	Bt average matrix	Mus in Grt	Mus average matrix	Pl average matrix	Grt average	Bt low Fe in Grt core	Bt high Fe in Grt rim	Bt average matrix	Mus in Grt	Mus average matrix	Pl average matrix
SiO$_2$	37.17	34.773	35.65	44.93	46.21	63.43	37.77	36.64	36.32	35.77	46.41	46.92	61.12
TiO$_2$	0.01	2.213	2.58	0.87	0.90	0.01	0.01	2.42	2.60	2.54	0.70	0.79	0.00
Al$_2$O$_3$	20.84	18.967	18.57	34.86	34.75	23.13	20.79	19.62	19.31	18.96	35.16	34.43	23.20
FeO^T	33.87	20.847	20.75	1.20	1.20	0.07	35.34	17.12	19.66	20.84	1.56	1.58	0.04
MnO	3.02	0.118	0.12	0.01	0.00	0.00	1.47	0.02	0.02	0.04	0.00	0.01	0.01
MgO	3.37	8.472	8.17	0.74	0.75	0.00	3.61	10.62	8.94	8.40	0.68	0.74	0.00
CaO	1.66	0.063	0.10	0.01	0.01	4.33	1.80	0.02	0.01	0.00	0.00	0.00	4.85
Na$_2$O	0.01	0.264	0.27	0.96	0.95	9.22	0.01	0.33	0.39	0.34	1.14	1.06	8.99
K$_2$O	0.00	7.581	7.68	8.83	8.89	0.09	0.00	8.90	8.60	8.77	9.43	9.50	0.14
Total	99.96	93.503	94.11	92.50	93.75	100.29	100.82	95.97	96.09	95.85	95.18	95.08	98.35
Si	3.00	5.16	5.50	6.13	6.21	2.80	3.01	5.47	5.47	5.45	6.18	6.24	2.76
Ti	0.00	0.25	0.30	0.09	0.09	0.00	0.00	0.27	0.29	0.29	0.07	0.08	0.00
Al	1.98	3.32	3.38	5.60	5.50	1.20	1.95	3.45	3.43	3.40	5.52	5.40	1.23
Fe	2.28	2.59	2.68	0.14	0.13	0.00	2.36	2.14	2.48	2.65	0.17	0.18	0.00
Mn	0.21	0.01	0.02	0.00	0.00	0.00	0.10	0.00	0.00	0.00	0.00	0.00	0.00
Mg	0.41	1.87	1.88	0.15	0.15	0.00	0.43	2.36	2.01	1.91	0.13	0.15	0.00
Ca	0.14	0.01	0.02	0.00	0.00	0.20	0.15	0.00	0.00	0.00	0.00	0.00	0.23
Na	0.00	0.08	0.08	0.25	0.25	0.79	0.00	0.10	0.11	0.10	0.29	0.27	0.79
K	0.00	1.44	1.51	1.53	1.52	0.00	0.00	1.70	1.65	1.71	1.60	1.61	0.01
Total	8.02	14.83	15.47	13.93	13.90	5.00	8.01	15.62	15.57	15.60	14.01	13.95	5.02

FeO^T is total FeO + Fe$_2$O$_3$.

40–60 μm in diameter. NIST-610 and 612 synthetic glasses were used as primary and secondary standards. Internal standardization was to CeO for monazite and CaO for garnet using values measured on the Cameca SX 100 electron microprobe at the Open University. Garnet analyses were visually screened for accessory phase interference: Zr for zircon (which contains HREE), Ti for rutile (which contains high concentrations of the high field strength elements) and P for monazite (high LREE) or apatite (high MREE) and any individual datasets with any of these elements at concentrations greater than an order of magnitude higher compared to the rest of the dataset were ignored. The monazite time-series signal was screened for changes in major elements such as Ca or Mg to assess the downhole thickness of the grain. REE concentrations were normalized to standard chondrite values (Palme & O'Neill 2014). 1σ uncertainty on the values, including reproducibility of an internal standard, is *c.* 5–10%.

Thermobarometry

PT conditions were calculated for assemblages in each sample that showed textural evidence for equilibrium at peak conditions. Garnet–biotite Fe–Mg exchange thermometry (Holdaway 2000) was applied to average compositions of matrix biotite (or, where present, inclusions of biotite in garnet) and garnet rims (avoiding the narrow post-peak re-equilibrated chemistry at the edges of the preserved garnets) to determine temperatures at peak conditions. Due to the 'flattening' of the major-element chemistry following prolonged residence at high temperatures, we acknowledge that the temperature thus obtained probably only represents a minimum estimate. For peak pressure, a calibration of the garnet–aluminium silicate–plagioclase–quartz (GASP) net transfer barometer based on the thermodynamic dataset of Holland & Powell (1998) was employed, supplemented by the garnet–biotite–muscovite–plagioclase net transfer barometer of Wu (2015) for two samples lacking aluminium silicate. Ti concentrations in biotite in different microstructural positions were used to calculate temperatures using two recent calibrations (Henry *et al.* 2005; Wu & Chen 2015).

U–Pb analyses

U–Th–Pb isotope data were collected *in situ* from monazites in polished thick sections at the NERC Isotope Geosciences Laboratory in Keyworth, UK using a Nu Instruments AttoM single collector sector-field ICP-MS with a New Wave UP193 (193 nm) Nd–YAG laser ablation system. Polished sections were placed into a 'large-format' New Wave Research cell with a washout time of *c.* 1 s.

U, Th, Pb and Hg isotopes were collected for 30 s using a laser spot size of 15–20 μm. Ablation was conducted at 5 Hz with a fluence of *c.* 2.5 J cm^{-2}.

Data processing used the time-resolved function on the Nu Instruments' software, an in-house Excel spreadsheet for data reduction and uncertainty propagation, and Isoplot for data presentation (Ludwig 2003). A standard sample-bracketing technique was used to correct the data. Unknowns were normalized to the reference monazite 'Manangotry' (554 Ma ID-TIMS age; Palin *et al.* 2013); 'Stern' and 'Moacyr' (512.1 ± 1.9 Ma and 515.6 ± 1.4 Ma ID-TIMS ages, respectively; Palin *et al.* 2013) were analysed to monitor accuracy and precision. Uncertainties were propagated following Horstwood *et al.* (2016) and include a contribution (as excess variance) from the external reproducibility of the reference material for the $^{207}Pb/^{206}Pb$, $^{206}Pb/^{238}U$ and $^{208}Pb/^{232}Th$ ratios. The external reproducibility of the final $^{206}Pb/^{238}U$ and $^{208}Pb/^{232}Th$ ages was *c.* 3% (2σ) and the accuracy of the ages is within 3% according to the secondary reference materials.

A ^{207}Pb-based common-lead correction was made using $^{207}Pb/^{206}Pb = 0.83 \pm 0.02$ (following the Stacey & Kramers 1975, Pb evolution model for a 20 Ma age) to calculate the proportion of common ^{206}Pb. A correction for excess ^{206}Pb used an assumed Th/U of 3 for average crust; we acknowledge that the Th/U available to monazite may not always closely resemble the whole-rock Th/U.

Results

Petrography and mineral chemistry

Metasedimentary GHS samples exposed in west and central Bhutan (Fig. 1) vary from garnet-mica schists to sillimanite- and kyanite-bearing gneisses depending on the relative abundance of mica and plagioclase. Compositional banding and a strong foliation are common. Summary major-element data are presented in Table 1. Garnet REE, monazite REE and sample photographs (field and thin section photomicrographs) are presented in the Supplementary material. Samples are described in sample number order.

LG-09-1. LG-09-1 is a metapelite collected from within a few kilometres of the contact with Paro metasediments along a road section east of Wangdue Phodrang in central Bhutan (Fig. 1). It contains major garnet, plagioclase, potassium feldspar, sillimanite, muscovite, biotite and quartz with accessory monazite, zircons, tourmaline, apatite and ilmenite (Fig. 2a). The matrix is dominated by <0.2–5 mm wide irregular bands that alternate between quartz-absent and quartz-dominant assemblages.

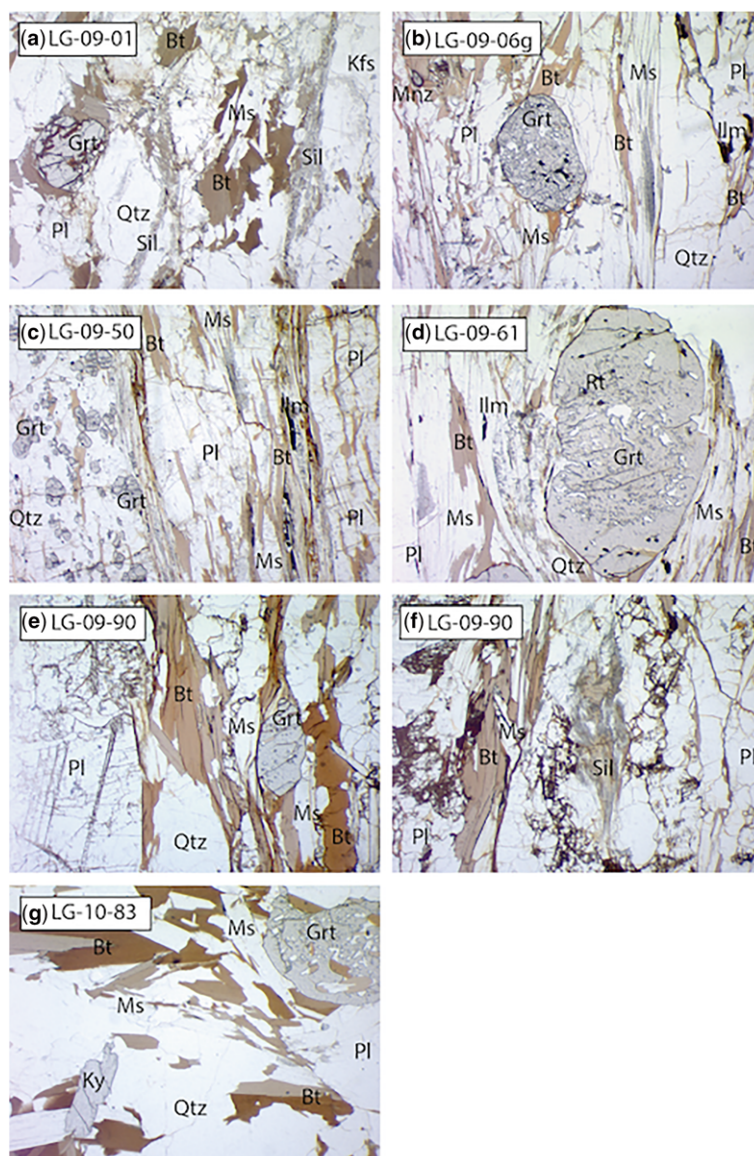Garnet porphyroblasts (*c.* 5% by volume) are <1 mm in diameter and sub-rounded, with inclusions

Fig. 2. Thin section photomicrographs. Mineral abbreviations after Whitney & Evans (2010): Bt, biotite; Grt, garnet; Kfsp, potassium feldspar; Ky, kyanite; Mus, muscovite; Pl, plagioclase; Qtz, quartz; Sill, sillimanite; Field of view 5.5 mm. Further images are available in the Supplementary material.

of randomly-distributed quartz. They preserve only weak major-element zoning, with average compositions of $Alm_{0.67}Spss_{0.17}Py_{0.11}Grs_{0.05}$ in the cores (Fig. 3a). Only minor concentration variations are recorded in the REE from core to rim, with the cores containing higher concentrations of HREE and similar concentrations of MREE compared to the rims (Fig. 4ai). The analysed garnet in this sample is more enriched in Mn, less enriched in Fe, more

enriched in HREE (>10 000 times chondrite compared to ∼<1000 times chondrite), and slightly depleted in MREE compared to the other samples in this study.

Plagioclase ($Ab_{0.74}$) is a common matrix phase and contains inclusions of quartz. Biotite ($X_{Fe} \approx 0.60$) is chemically unzoned, although muscovite grains are zoned from $X_{Fe} \approx 0.62$–0.68 from core to rim (both along and across cleavage).
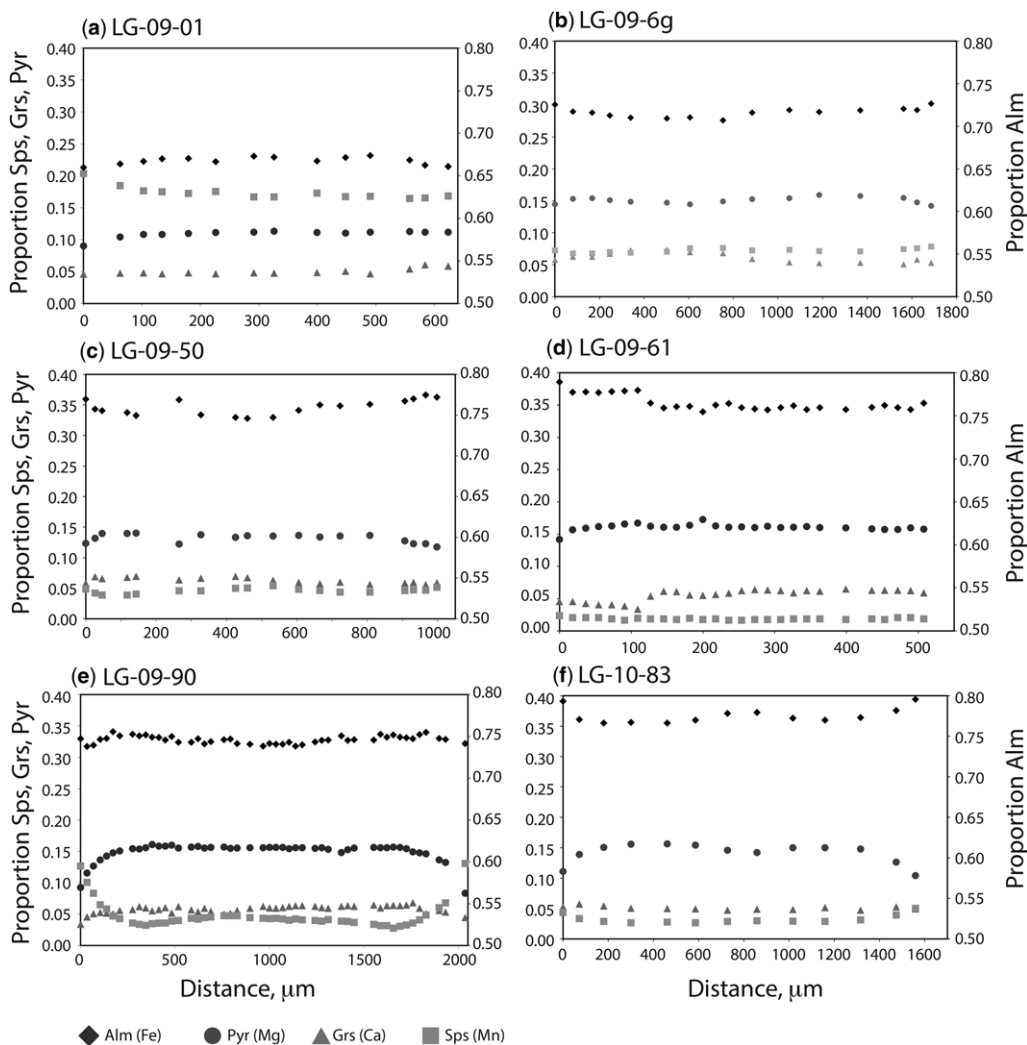
Fig. 3. Major element profiles across typical garnets in all samples.

Monazite grains are only found in the matrix and are 20–150 μm in diameter. Many grains show distinct core–rim zoning in Y, with sharp zone boundaries. However, these zones are commonly irregular and patchy (Fig. 5). The <50 μm wide rims yield higher Y and HREE concentrations than the cores (Fig. 4aii).

LG-09-6g. LG-09-6g is a schist collected from the road section west of Trongsa in central Bhutan (Fig. 1) that contains the major phases garnet, plagioclase, muscovite, biotite, and quartz, with accessory monazite, zircon, tourmaline and ilmenite (Fig. 2b). Garnet porphyroblasts (*c.* 5% by volume) are <3 mm in diameter and sub-rounded. Inclusions are common

and randomly distributed. Garnet is only weakly zoned in major elements (Fig. 3b), with average core composition of $Alm_{0.72}Py_{0.15}Spss_{0.07}Grs_{0.06}$. Garnets show no obvious zoning in HREE concentrations from core to the rim but there is a significant rim enrichment in the MREE (Fig. 4bi).

Biotite forms elongate laths within mica-rich layers orientated parallel to the pervasive foliation ($X_{Fe} \approx 0.49$). Biotite inclusions in garnet vary from $X_{Fe} \approx 0.36–0.50$. Muscovite is fine-grained and is fabric-defining within the mica-rich layers. Grains in the quartz-rich regions form mats of smaller subgrains. Matrix muscovite has composition $X_{Fe} \approx 0.41$, whereas muscovite inclusions in garnet yield $X_{Fe} \approx 0.45$. Matrix plagioclase has
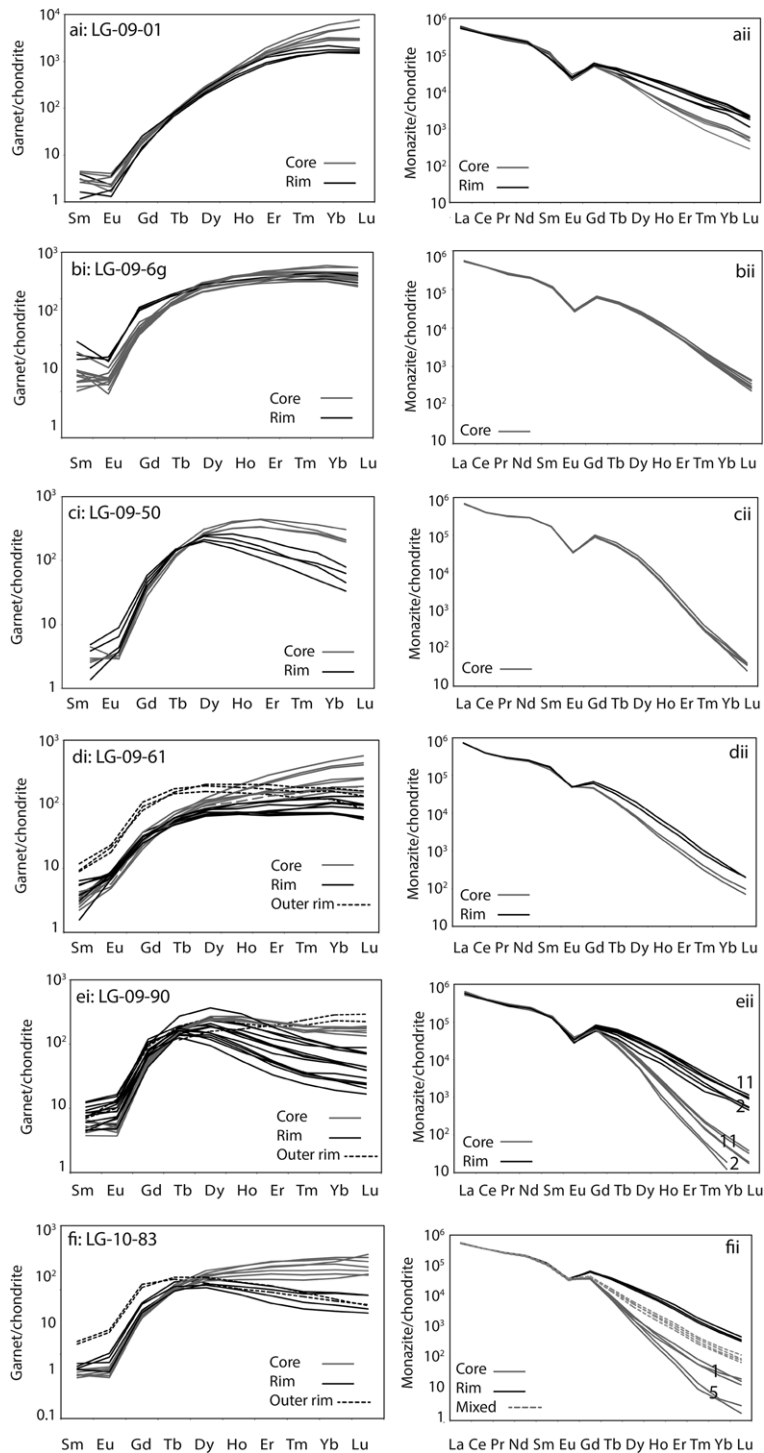
Fig. 4. REE data. (i) Garnet REE profiles normalized to chondrite concentrations (Palme & O'Neill 2014). (ii) Monazite REE profiles normalized to chondrite concentrations. Numbers indicate the grain numbers analysed (see Supplementary material Table 4).
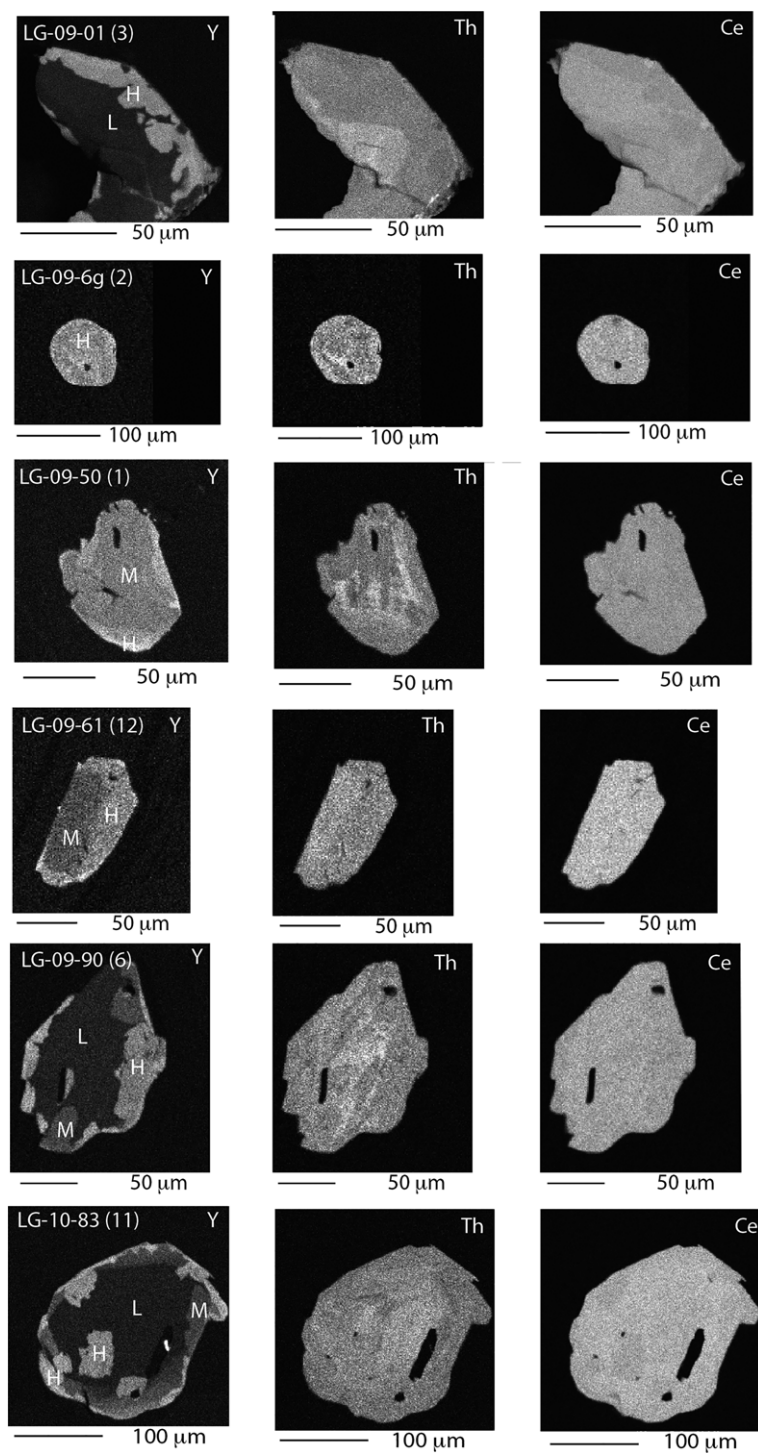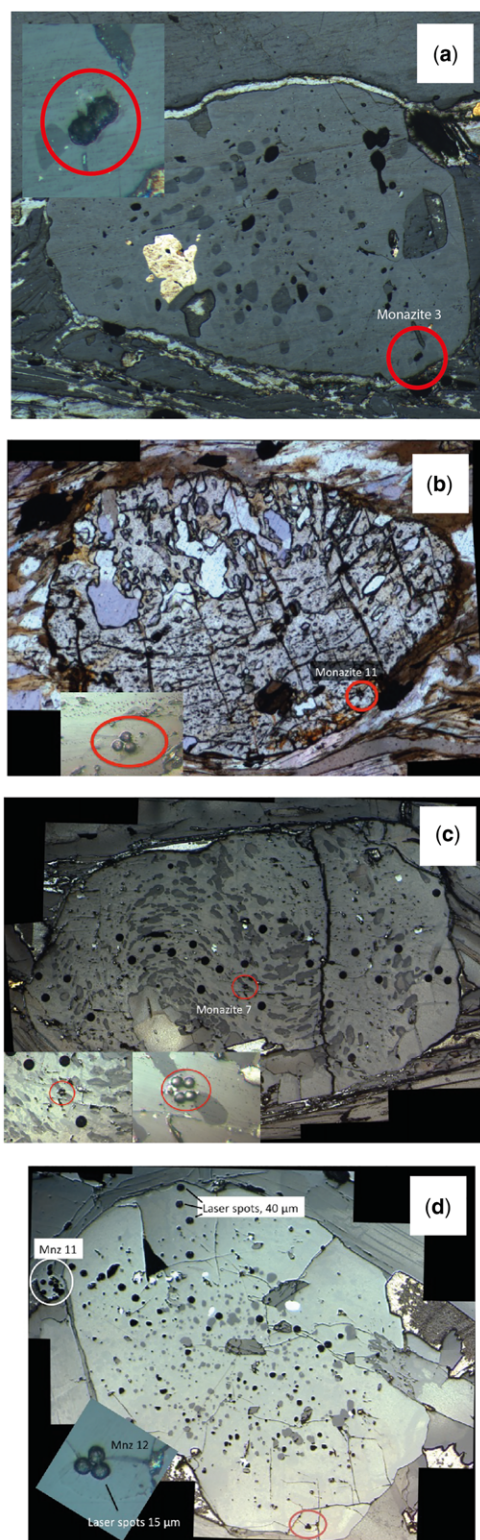
Fig. 5. Y, Th and Ce concentration maps of typical monazite grains in each sample. For the Y maps: H, relatively high concentration; M, relatively medium concentration; L, relatively low concentration. The greyscale is common to all images. The number in parentheses after the sample name is the grain number (see Supplementary material Table 4).

composition $Ab_{0.77}$, whereas inclusions in garnet vary from $Ab_{0.52-0.74}$.

Matrix monazites are 10–150 μm in diameter, with inclusions in garnet generally <20 μm (Fig. 6a) Matrix grains are chemically unzoned, with average Th, Ce and Y concentrations (Fig. 5), and relatively flat chondrite-normalized HREE patterns (Fig. 4bii).

LG-09-50. LG-09-50 is a metapelite sampled along the road near Surey in south-central Bhutan (Fig. 1). It contains major garnet, plagioclase, biotite, muscovite and quartz, with accessory monazite, zircon, tourmaline and ilmenite. Muscovite and biotite are commonly intergrown and define the foliation, along with elongate quartz and plagioclase grains (Fig. 2c). Garnets measuring <700 μm in diameter are concentrated in distinct layers and form *c.* 3% of the sampled volume. They contain randomly-oriented inclusions of quartz, plagioclase, ilmenite and biotite, and do not preserve significant major-element zonation (Fig. 3c). The average core composition is $Alm_{0.76}Py_{0.13}Grs_{0.06}Sps_{0.04}$. HREE concentrations decrease significantly and MREE concentrations increase slightly from core to rim (Fig. 4ci).

Plagioclase grains are internally homogeneous; however, matrix grains have higher Na concentrations ($Ab_{0.79}$) than those included in garnet ($Ab_{0.73}$). Matrix muscovite and biotite are unzoned, with compositions of $X_{Fe} \approx 0.45$ and $X_{Fe} \approx 0.53$ respectively.

Monazites are 20–120 μm in diameter and are only found in the matrix. Rims <20 μm wide have higher Y concentrations than the cores (Fig. 5). Only the cores were large enough to measure the REE concentrations by laser ablation, and these show steep chondrite-normalized HREE patterns (Fig. 4cii).

Fig. 6. Monazite inclusions in garnet. (**a**) Stitched reflected light photomicrograph mosaic of a garnet in sample LG-09-6g showing monazite inclusion in the garnet rim. The garnet is 2 mm long and the laser pits in monazite are 15 μm in diameter. (**b**) Stitched plane polarized light photomicrograph mosaic of a garnet in LG-09-61 showing a monazite inclusion in the rim (inset photo taken in reflected light). The garnet is 2.2 mm long and the laser pits in monazite are 15 μm in diameter. (**c**) Stitched reflected light photomicrograph mosaic of a second garnet in LG-09-61 showing a monazite inclusion in the garnet core. The garnet is 2.3 mm long. The garnet laser pits are 40 μm diameter and the monazite laser pits are 15 μm diameter. (**d**) Stitched reflected light photomicrograph mosaic of garnet in LG-10-83 showing a monazite inclusion in the garnet rim. The garnet is 1.9 mm long. The garnet laser pits are 40 μm diameter and the monazite laser pits are 15 μm diameter.

LG-09-61. LG-09-61 is a schist collected from the basal GHS *c.* 8.5 km NW of Sarpang, south-central Bhutan (Fig. 1) It contains major garnet, plagioclase, muscovite, biotite and quartz with accessory monazite, zircon, tourmaline, ilmenite, rutile and apatite. Garnet porphyroblasts up to 2×4 mm across are subhedral to rounded and make up *c.* 20% of the sample volume. Inclusions of quartz, staurolite, ilmenite, biotite, rutile and muscovite are common in the garnet cores. Garnet microstructures record at least three phases of growth: quartz and rutile define sigmoidal inclusion trails in the garnet cores, truncated by inclusion-poor rims <0.5 mm wide. The core and the inner rim have identical major-element chemistry ($Alm_{0.76}Py_{0.16}Grs_{0.06}Spss_{0.02;}$ Fig. 3d). The grains are overgrown by a slightly higher-iron, lower-calcium outer rim ($Alm_{0.78}Py_{0.16}$-$Grs_{0.04}Spss_{0.02}$) with ilmenite inclusions on faces perpendicular to the foliation. These three growth phases are also recorded in the REEs. HREE concentrations decrease from core through the inner rim, then increase towards the outer rim (Fig. 4di). MREE concentrations in the core and inner rim are very similar but are higher in the outer rim.

Biotite ($X_{Fe} \approx 0.55$) and muscovite ($X_{Fe} \approx 0.42$) define the foliation, which wraps the garnet; these minerals also occupy the garnet pressure shadows. Biotite and muscovite inclusions in garnet are chemically distinct from matrix grains at $X_{Fe} \approx 0.38$–0.46, and $X_{Fe} \approx 0.46$ respectively.

Matrix plagioclase ($Ab_{0.87}$) forms anhedral, cracked grains $<0.5 \times 2$ mm in size. Staurolite inclusions in garnet vary from $X_{Fe} \approx 0.66$–0.86, and there appears to be no link between chemistry and distance to the rim of the garnet. Fluoro-apatite forms anhedral, cracked grains, <400 μm across, within the matrix and as inclusions in garnet. Quartz forms ribbons within the matrix; grains are deformed into subgrains of various sizes. Matrix ilmenite (<200 μm in diameter) is commonly cored by rutile.

Matrix monazites are *c.* 100 μm in diameter, with smaller grains included in garnet (20–40 μm in diameter). The <20 μm wide rims yield higher Y concentrations than the cores (Fig. 5). Three monazites included in garnet were analysed (Fig. 6b, c). Matrix monazites show greater HREE enrichment in their rims than their cores and show intermediate steepness HREE patterns (Fig. 4dii).

LG-09-90. LG-09-90 is a schist that was collected along a trekking route *c.* 2 km south of Semtoka within a few hundred metres of the basal GHS–Paro metasediment contact in the Paro window (Fig. 1). It contains major garnet, sillimanite, plagioclase, biotite, muscovite and quartz, minor chlorite and tourmaline, and accessory monazite, zircon, rutile and ilmenite. Garnet porphyroblasts <2 mm across are rounded, fractured and contain inclusions of quartz, biotite, muscovite, chlorite, tourmaline and rutile. They form *c.* 10% of the sample volume. Grains are generally only weakly zoned in major elements, with a composition of $Alm_{0.75}Py_{0.13}Grs_{0.05}Spss_{0.07}$ (Fig. 3e). Their HREE concentrations decrease from core to rim, but outer rims are comparatively enriched. The MREE concentrations are slightly lower in the cores than in the rims (Fig. 4ei).

Biotite ($X_{Fe} \approx 0.59$) and muscovite ($X_{Fe} \approx 0.47$) form narrow laths parallel to foliation, and wrapping garnets. Inclusions of biotite and muscovite in garnet have similar composition to matrix grains. Plagioclase (Ab_{79}) is unzoned and contains inclusions of muscovite and quartz. Fibrolitic sillimanite forms bundles parallel to the foliation associated with biotite.

Matrix monazite grains are 50–150 μm in diameter. They show patchy zoning with either one or two different higher-Y rim compositions on low Y cores (Fig. 5). Different grains yield different absolute REE concentrations but overall the rims are more enriched in the HREE than the cores, with considerably steeper HREE patterns yielded by the cores than rims (Fig. 4eii).

LG-10-83. LG-10-83 was collected from within the GHS structurally below a synform of metasediments along the road near Chukha in SW Bhutan (Fig. 1). The sample contains major garnet, kyanite, plagioclase, biotite, muscovite and quartz with accessory monazite, zircon, apatite, ilmenite and rutile. Garnets (*c.* 10% of the sample volume) are <2 mm across and subhedral to rounded. Inclusions of quartz, biotite, apatite, rutile and muscovite are randomly orientated, and are relatively absent in the outer 200 μm. Garnet shows only subtle major-element chemical zoning, with an average core composition of $Alm_{0.78}Py_{0.14}Grs_{0.05}Sps_{0.03}$ (Fig. 3f). HREE are enriched in the cores compared to the rims, and MREE are comparatively enriched in the rims, especially the outer rims (Fig. 4fi).

Biotite is unzoned but shows distinct chemical variation between microstructural position: $X_{Fe} \approx 0.58$ in the matrix, and $X_{Fe} \approx 0.47$–0.55 in garnet. Muscovite shows similar composition of $X_{Fe} \approx 0.55$ in both the matrix and in garnet. Plagioclase is (Ab_{76}) and not chemically zoned.

Matrix monazites and those included in kyanite are *c.* 100–200 μm in diameter, with smaller grains included in garnet (<50 μm; Fig. 6d). The cores of matrix grains and those included in kyanite yield average Ce and Th concentrations and relatively low to average Y concentrations (Fig. 5). Rims on matrix monazites, <20 μm wide, contain higher Y concentrations. Inclusions in the garnet rim showed average Ce and Th and relatively low to average Y concentrations, similar to the matrix grain cores.

Different matrix grains yield different absolute REE concentrations but overall the rims are more enriched in the HREE than the cores and show flatter HREE patterns (Fig. 4fii).

Summary of garnet REE results. Garnets in all samples yield 'typical' patterns of higher HREE and lower MREE concentrations (Fig. 5). All samples show an increase in MREE concentrations from core to rim and (apart from LG-09-6g) a decrease in HREE concentrations from core to rim. The garnet cores in samples LG-09-01 and LG-09-61 show increasing HREE concentrations from Ho to Lu. The garnet cores in samples LG-09-6g, LG-09-90 and LG-10-83 show similar HREE concentrations from Ho to Lu, whereas the cores of LG-09-50 garnet show decreasing HREE concentrations. Garnet rims in samples LG-09-50 and LG-90-90, and the outermost rims of samples LG-09-61 and LG-10-83 show decreasing HREE concentrations from Ho to Lu.

Concentrations of the MREE are variable across the different samples: hump-shaped patterns due to enrichment in the MREEs are apparent in the rims of LG-09-50 and LG-09-90 and the outer rims of LG-09-61 and LG-10-83.

Summary monazite REE results. All monazites for which separate core and rim REE data were obtained show similar concentrations of LREE in both, but variable concentrations (and steepness of chondrite-normalized patterns) in the HREEs. All samples show enrichment of Y and HREE in the rims compared to the cores. All grains yield negative Eu anomalies, but samples LG-09-61 and LG-10-83 yield reduced negative anomalies compared to other samples. Samples with analysable cores and rims (LG-09-61, LG-09-90 and LG-10-83) show a reduction in the negative Eu anomalies from core to rim (*c.* 0.5–0.6 to 0.3; caused by changes in the concentration of Gd rather than an overall change in the concentration of Eu, see Fig. 4). Gd/Lu ratios in monazites with separate cores and rims yield high and variable core values (180 000–500), with lower and more consistent rim values (2500–200).

PT determinations

All samples yielded overlapping garnet–biotite temperatures from 620°C to 670°C and overlapping pressures from 5.8 to 10.1 kbar. Uncertainties are estimated at *c.* 35°C (Holdaway 2000; Wu & Cheng 2006) and 1.2 kbar (cited in Holland & Powell 1998). Results are displayed in Table 2 and average temperatures are plotted on Figure 7. In general, Ti concentrations in biotite suggest crystallization temperatures of *c.* 570–680°C with some

Table 2. *PT results for all samples*

Sample	T*(°C)	P[†](kbar)	Ti in Bt[‡](°C)
LG-09-01	666	5.8	683–645
LG-09-6g	624	6.7	642–567
LG-09-50	619	*7.3*	609–573
LG-09-61	665	*10.1*	634–386
LG-09-90	666	7.0	645–612
LG-10-83	663	7.3	654–634

*Grt–Bt: Holdaway (2000).
[†]GASP: Holland & Powell (1998) except samples LG-09-50 and LG-09-61, GBMP: Wu (2015).
[‡]Henry *et al.* (2005).

scatter. Inclusions of biotite in garnet commonly yield temperatures similar to matrix biotite grains. Ti-in-biotite temperatures are generally lower than the temperatures calculated by the garnet–biotite method.

Geochronology

Monazite in most samples yielded a range of ages rather than a single population (Fig. 8). In two samples, monazites included in garnet and kyanite yielded ages that were similar to the ages of matrix grain cores. The spread in age of the monazite cores and inclusions in garnet and kyanite was considerably smaller than the spread yielded by the matrix monazite rims.

We present U–Pb ages; [232]Th–[208]Pb ages were also measured but are slightly less precise due to the nature of the data collection protocol. These ages are not affected by any disequilibrium of intermediate daughter isotopes like in the [238]U–[206]Pb system. With few exceptions, the [232]Th–[208]Pb and [206]Pb-excess-corrected [206]Pb–[238]U ages are within uncertainty of each other for individual analyses, with the mean difference of *c.* 200 pairs of analyses being 0.6 ± 1.1 Ma. The two sets of dates also preserved the relative difference in age when considered within the petrographic context and thus support the interpretations presented. These data are all tabulated in Supplementary material tables.

Nine analyses from three monazite cores in LG-09-1 yielded ages from 19–16 Ma (Fig. 8a). Seven out of eight analyses of the high-Ce patches in four grain cores yielded a lower intercept age (regressed with a common lead [207]Pb/[206]Pb composition of 0.83 ± 0.02; see Methods) of 19.3 ± 0.3 Ma, MSWD = 0.56. Fifteen analyses of four grain rims yielded ages from 17.2 to 14.5 Ma.

Thirty-three analyses from six monazite grains in LG-09-6 g yielded ages between 24.5 and 20.5 Ma (Fig. 8b). Two analyses from a single grain in a garnet rim yielded ages similar to the youngest matrix grains.

Fig. 7. Temperature results for all samples, calculated using the garnet–biotite thermometer (Holdaway 2000) and the Ti-in-biotite thermometer (Henry *et al.* 2005; Wu & Chen 2015).

Twenty-four analyses from six grains in LG-09-50 yielded an age of 22.0 ± 0.16 Ma, MSWD = 1.4 (Fig. 8c). Of the two rim analyses, one yielded a similar age to the 'core' group, and the other yielded a younger age of *c.* 19 Ma.

Twelve analyses from five monazite cores in LG-09-61 yielded a range in ages between 22.4 and 19.5 Ma. (Fig. 8d). Nine analyses from three grain rims yielded ages between 19.1 and 17.1 Ma. Seven analyses from the three grains included in garnet (two from the garnet core and one near the rim) yielded a range of ages between 23.0 and 20.3 Ma.

Fifteen analyses from three monazite cores in LG-09-90 yielded a range of ages between 24.0 and 21.8 Ma (Fig. 8e). Sixteen of 24 analyses from six grain rims yielded a range of ages between 19.2 and 15.2 Ma. Four rim analyses yielded ages that overlap with ages yielded by the cores.

Thirteen analyses from two grain cores plus nine analyses from a single inclusion in kyanite in LG-10-83 yielded a regressed age of 21.0 ± 0.2 Ma, MSWD = 0.58 (Fig. 8f). Eighteen analyses from five matrix rims yielded ages between 18.8 and 13.6 Ma. Three data points on two inclusions in the garnet rim yielded ages of 21 Ma (2 analyses) and 19.7 Ma.

Summary geochronology results. Pelitic gneiss samples from central Bhutan contain chemically zoned monazites that yield ages between 24.5 and 13.6 Ma. Monazites included in garnet and kyanite

yield ages between 23.0 and 20.3 Ma, lower-Y matrix monazite cores yield ages between 24.5 and 19.5 Ma and higher-Y matrix monazite rims yield ages between 19.2 and 13.6 Ma.

Discussion

Garnet growth, resorption and re-equilibration

Garnets in some samples show petrographic and trace element evidence for a complex growth and resorption history. Relatively inclusion-free outer rims of different major and trace element composition that align with the foliation have overgrown inclusion-rich cores and inner rims in samples LG-09-61 and LG-10-83 (Fig. 2d). Garnets in LG-10-83 also show evidence for uneven breakdown of some grains after the outer rims have formed.

The major-element profiles across all samples apart from LG-09-61a are relatively flat except at the outermost rim. The flat profiles suggest re-equilibration by diffusion of the major elements within the garnet during prolonged residence at high temperatures (e.g. Woodsworth 1977). The minor zoning measured at the edges of many of the grains suggests limited re-equilibration with the matrix during retrogression (e.g. Frost & Chacko 1989).

The REE profiles across all samples show systematic variations that suggest that the REE have not been
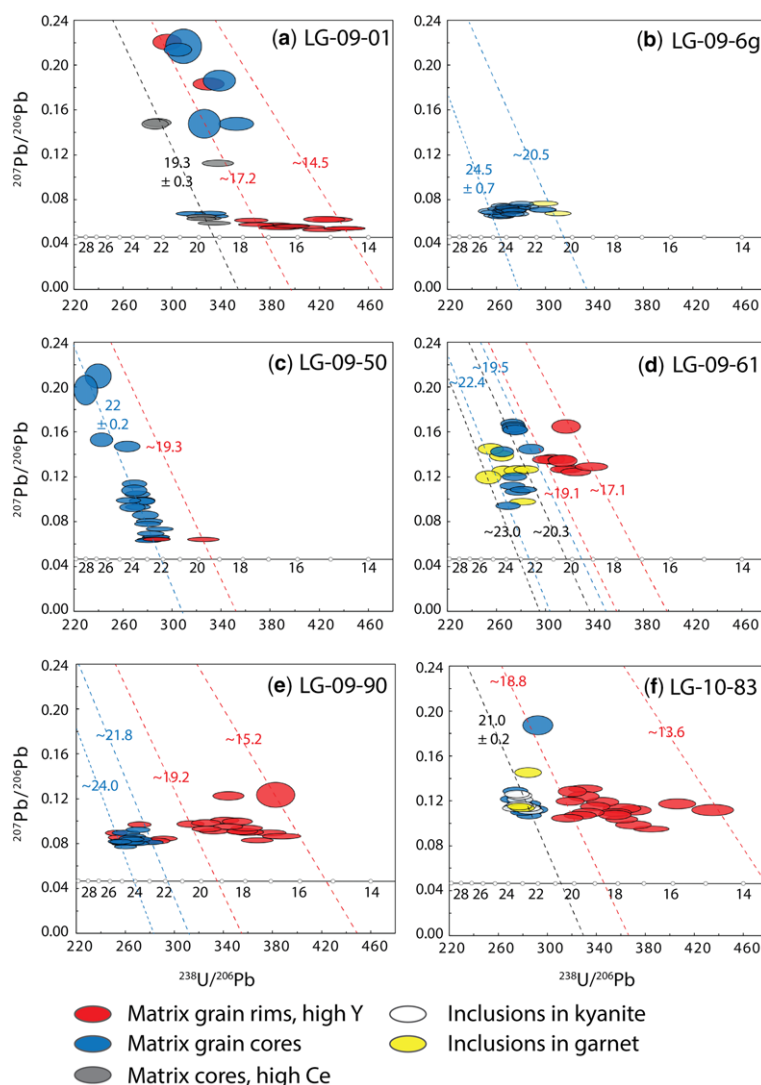
Fig. 8. Monazite Tera-Wasserburg U–Pb age plots.

significantly disturbed since the garnets grew. The laser ablation profiles were sited across the best-preserved garnets in each sample, such that the chemical core of the grain was captured in each profile. We recognize, however, that due to 3D effects of thin-sectioning we may not have captured the true cores of any of the grains during the acquisition of the profiles.

Thermobarometry

Maximum temperatures recorded by all samples lie between *c.* 600 and 700°C, at pressures between 7 and 10 kbar, consistent with upper amphibolite-facies conditions. Apart from in sample LG-09-01, the calculated Grt–Bt temperatures generally lie at the upper end of, or are higher than, the Ti-in-biotite (TiB) temperatures. We interpret the homogeneous major-element compositions in garnet as the result of thermal re-equilibration of the major elements during the metamorphic peak; no major-element record of prograde garnet growth remains. The yielded Grt–Bt temperatures are therefore interpreted as the temperatures at which thermal equilibration was reached, between *c.* 620 and 670°C. The TiB temperatures for biotite inclusions in garnet

generally overlap temperatures recorded in matrix grains, suggesting either garnet and matrix biotite growth during similar conditions or thermal re-equilibration in biotite. Published PT estimates from central Bhutan from the same or nearby localities provide similar results (Corrie *et al.* 2012).

Monazite growth, resorption and re-equilibration

None of the monazites in our samples show euhedral crystal faces and concentric chemical zoning patterns. This indicates that they have all experienced several episodes of growth and resorption during the metamorphic cycle. The aim of our sampling strategy was to collect U–Pb and REE data from each of the different chemical zones represented in each rock.

Scattering of monazite U–Pb ages, as demonstrated in Figure 8, is a common feature in Himalayan samples (e.g. Warren *et al.* 2011; Tobgay *et al.* 2012). This scatter either reflects the time frame over which monazite grew (monazite-forming reactions in metapelites are still poorly constrained e.g. Simpson *et al.* 2000; Corrie & Kohn 2008; Janots *et al.* 2008), post-growth disturbance by fluids (e.g. Seydoux-Guillaume *et al.* 2012) or analytical artefact due to low radiogenic lead concentrations or mixing of zones of different age. As the chemical composition of the monazite rims in all samples is uniform, we feel that the scatter in the monazite rim ages (Fig. 8) is most likely due to monazite growth over a long time period rather than analytical mixing of older core ages with younger rims (although this cannot be completely ruled out in these samples). Apart from in sample LG-09-01, the scatter in the monazite core ages is smaller than the scatter in the rim ages, over 1–2 Ma in most samples. Within analytical uncertainty, the monazite core ages in this study overlap with the ages of the monazite included in garnet.

Some of the monazite cores show patchy zoning in Th (Fig. 5) that could suggest alteration by fluids after growth (e.g. Kelly *et al.* 2012). These grains yield the same trends in REE concentrations as grains that do not show this patchy alteration (Fig. 4). Since this patchiness does not appear to be linked either to age or increased age scatter (Fig. 8), we do not feel that the monazite grains have been significantly chemically altered after growth.

REE and Y concentrations in garnet and monazite

Different major and accessory phases in metapelites have varying affinities for trace elements such as Y and the REEs. As such, their concentrations, and intra-grain variations can be used as a 'fingerprint'

for equilibrium if their partitioning behaviour is well understood.

Trace-element zoning patterns in garnet are controlled by the availability of the element in the matrix (e.g. from the coeval breakdown of other phases), the rate of transport of that element through the matrix towards the growing garnet and competition for that element from other phases (e.g. Skora *et al.* 2006). The breakdown of other minerals in the matrix that contain the trace elements of interest may provide an explanation for the zonal enrichments seen in some samples. For example, apatite is an important host of MREE, and its breakdown may have contributed to the MREE enrichment seen in the garnet rims of LG-09-61 and LG-10-83 (Fig. 4di, fi). Apatite is still present in the matrix of both samples. K-feldspar and plagioclase are important hosts for Eu, and the negative Eu anomaly seen in all garnet and monazite REE patterns here indicates that both grew in the presence of feldspar (an observation corroborated by the presence of feldspar in all analysed samples).

Th/U ratios do not vary systematically from core to rim in the monazites. In samples LG-09-6g and LG-09-90 the Th/U range is narrow, from *c.* 8 to 12. In sample LG-10-83 Th/U the matrix monazite rims yield a higher range, from 8 to 16, whereas in LG-09-61 it is the monazite included in garnet that yields the higher range. In LG-09-50 a single grain (monazite 2) yields a consistently higher Th/U (16–18) than the other grains (6–10). In sample LG-09-01 high-Ce cores yield a narrower range of Th/U ratios (8–10) than the rest of the grains. These Th/U ratios are similar to those reported by Rubatto *et al.* (2006). We do not see the strong increase in Th/U in the monazite rims (up to values of 50) reported by Rubatto *et al.* (2006) and interpreted in that study as being caused by co-crystallizing zircon competing for U.

Many monazites from the GHS exhibit high Y rims overgrowing lower Y cores or mantles (e.g. Foster *et al.* 2002; Kohn *et al.* 2005; Tobgay *et al.* 2012; Rubatto *et al.* 2013; Zeiger *et al.* 2015). Increasing enrichment in Y and HREE in monazite rims has been interpreted as evidence for garnet breakdown (garnet generally being the main reactive host of Y and REE in major phases from Himalayan rocks; e.g. Harris *et al.* 1992) during partial melting or sub-solidus decompression and exhumation in the presence of fluid (Pyle & Spear 2003; Kohn *et al.* 2005). The chemically-distinct garnet outer rims that are aligned with the foliation in samples LG-09-61, 90 and 10–83 suggest garnet growth occurred contemporaneously with deformation. The discontinuous nature of these outer rims, and the discontinuity of the inclusion patterns in many of our samples suggests irregular garnet breakdown, most likely during decompression and exhumation.

Coeval crystallization of monazite and garnet?

Monazite inclusions were present in garnet in three samples: LG-09-6g, LG-09-61 and LG-10-83 (Figs 6, 8). In all cases the included grains yielded U–Pb ages that overlap with the ages of the matrix core population. In samples LG-09-61 and LG-10-83 the matrix monazite rims post-date the population included in garnet, suggesting that the rims grew after the garnets had stopped growing. Furthermore, the high-Y rims on the matrix monazites in many of the samples suggest growth during garnet breakdown. These monazite rims cannot therefore have formed in equilibrium with the garnets.

Monazite REE data were not collected from monazite inclusions in the garnet because their small size meant that it was nearly impossible to ensure that only monazite (and not garnet) was ablated. In most cases the grains had anyway already mostly been destroyed by the U–Pb data acquisition. However, the inclusion relationships, overlapping ages and higher Gd/Lu ratios in all analysed matrix monazite cores compared to the rims suggest growth in the presence of garnet (e.g. Hermann & Rubatto 2003; Regis et al. 2016).

Due to the presence of monazite inclusions in the garnet inner rims (but not in the chemically distinct outer rims) in samples LG-09-6g, LG-09-61 and LG-10-83, we suggest that the chemical composition of the matrix monazite cores reflects the composition of monazite that grew in equilibrium with the garnet rims. Figure 9 shows the matrix monazite core/garnet rim data from our samples plotted against the previously reported trends (Ayres & Harris 1997; Hermann & Rubatto 2003; Buick et al. 2006); Table 3 reports the mean values of our dataset. Our data show a stronger enrichment in HREE

Table 3. *Garnet–monazite distribution coefficients calculated from the mean of the sample matrix monazite core/garnet rim compositions*

	Value	Std dev
Sm	28 980	16 430
Eu	6560	2610
Gd	1580	730
Tb	360	170
Dy	94	38
Ho	31	11
Er	11	3.4
Tm	4	1.2
Yb	2	0.6
Lu	1	0.3

in garnet and similar MREE enrichment in monazite compared to the previous studies. Overall our data show a steeper garnet–monazite REE relationship. As REE partitioning behaviour between garnet and monazite in natural systems may provide a 'fingerprint' of equilibration and hence a way of linking monazite age to metamorphic stage via garnet growth, the discrepancy between our and previously reported datasets warrants investigation.

Factors that may have influenced garnet–monazite partitioning behaviour

The discrepancy between our dataset and the previously reported datasets may be due to one or more of the following factors (Table 4): analytical artefacts (for example an over-estimation of the concentrations of low-abundance elements); disequilibrium (in any of the previously-reported studies or this study, as none of the datasets are based on experimental data); varying PT conditions; presence/absence of melt or hydrous phase; competition for REE by another co-crystallizing REE-bearing phase (such as zircon or apatite); or the major-element composition of garnet and/or monazite.

Although concentrations of MREE in garnet and HREE in monazite were low, they were always within detection limits. Uncertainty on the measurements is 5–10%. We therefore consider our analyses to be robust, and conclude that the difference in slope between our data and previously reported data is not due to analytical artefacts.

Equilibrium partitioning between phases during sub-solidus metamorphism requires efficient mobility of the requisite elements to the growing crystal face. Differences in trace-element composition of otherwise similarly-zoned monazites in samples LG-09-90 and LG-10-83 suggest that equilibrium may only have been very locally achieved in some of our samples. In both samples, the composition
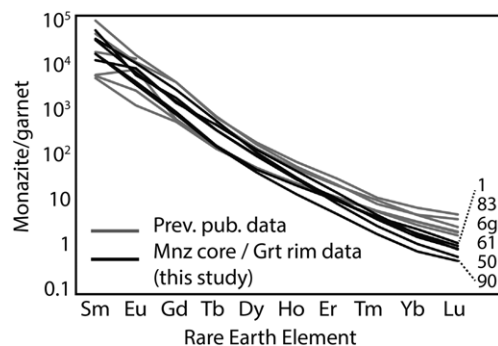

Fig. 9. Relationship between matrix monazite core REE compositons v. garnet rim (not outer rim) REE compositions (black). Sample numbers are identified on the right. Previously published data (grey) from Hermann & Rubatto (2003), Buick et al. (2006) and Rubatto et al. (2006).

Table 4. *Confounding factors that might affect partitioning behaviour between garnet and monazite*

Sample ID	P (kbar)	T (°C)	Garnet composition	Assemblage	Melt presence	Bulk rock
P-FS 108*	9–11	700–800	Alm 66% Pyp 26–28% Grs 3–4% Sps 2%	Grt–Ky–Qtz–Pl–Bt– Rt–Zrn–Mnz–Po	Yes	Al-rich, SiO$_2$-poor pelitic granulite
SGP3[†]	3.3–4.0	775–785	Alm 80% Pyp 13% Grs 3–4% Sps 3–4%	Kfs–Qtz–Pl–Crd–Bt– Grt–Opx–Spl–Opm– Zrn–Mnz	Yes	Metapelite
SGL5[†]	4	800–810	Alm 84–85% Pyp 9–11% Grs 3% Sps 2%	Kfs–Qtz-Pl–Crd–Bt– Grt–Ttn–Opm– Zrn–Mnz	Yes	Metapsammite
SGM5[†]	4	800–810	Alm 83–84% Pyp 10–12% Grs 3% Sps 3%	Kfs–Qtz–Crd–Bt–Grt–Opx–Spn–Opm– Zrn– Mnz	Yes	Metapsammite
98 Ma-55[‡]	*8–10*	790–810	Alm 62–74% Pyp 23–25% Grs 1.5–2.5% Sps 0.5–1.0%	Grt–Crd–Bt–Qtz–Sil– Spl–Oam–Rt–Ilm– Zrn–Mnz–Aln–St	No	SiO$_2$-rich gneiss
LG-09-1[§]	5.8	666	Alm 67% Pyp 9–11% Grs 5% Sps 17–20%	Grt–Ky–Sil–Qtz–Pl– Kfs–Bt–Ms–Ilm–Ap– Zrn–Mnz	Possibly	Pelitic gneiss
LG-09-6g[§]	6.7	624	Alm 75–76% Pyp 13–14% Grs 2–5% Sps 3–6%	Grt–Ky–Sil–St–Qtz–Pl–Bt–Ms–Tur–Ilm–Zrn–Mnz	No	Pelitic gneiss
LG-09-50[§]	7.3	619	Alm 75% Pyp 13% Grs 6% Sps 4%	Grt–Qtz–Bt–Ms–Pl– Tur–Ilm–Zrn–Mnz	No	Pelitic schist
LG-09-61[§]	10.1	665	Alm 77% Pyp 14–16% Grs 5% Sps 2%	Grt–Qtz–Pl–Bt–Ms– St(in Grt)–Ilm–Rt– Tur–Ap–Zrn–Mnz	No	Pelitic gneiss
LG-09-90[§]	7.0	666	Alm 74–75% Pyp 9–16% Grs 4–6% Sps 4–13%	Grt–Sil–Qtz–Pl–Bt–Ms–Ilm–Rt–Tur–Zrn–Mnz	No	Pelitic schist
LG-10-83[§]	7.3	663	Alm 77–79% Pyp 11–15% Grs 5% Sps 3–5%	Grt–Ky–Qtz–Pl–Bt–Ms–Ilm–Rt–Ap–Zrn–Mnz	No	Pelitic schist

*Hermann & Rubatto (2003).
[†]Rubatto *et al.* (2006).
[‡]Buick *et al.* (2006) (P values extrapolated from nearby samples).
[§]this study.
Mineral abbreviations follow Whitney & Evans (2010) apart from Oam and Opm (as written in original papers) which we take to reflect orthoamphibole and opaque minerals.

of the monazite that was located closest to the analysed garnet was used for comparison.

Our samples reached lower peak temperatures but similar pressures to the previously reported studies, at c. 650–750°C and 6.5–8.5 kbar, compared with 700–800°C, 10 kbar for the Val Malenco (Hermann & Rubatto 2003), 775–810°C, 3–4 kbar for Mount Stafford (Rubatto et al. 2006) and 800°C, 8–10 kbar for the Central Limpopo Belt, South Africa (Buick et al. 2006; Table 4). In Val Malenco and Mount Stafford, garnet and monazite equilibrated in the presence of melt. In this study, only one sample (LG-09-01) shows petrographic evidence for partial melting (presence of K-feldspar, replacement of biotite by sillimanite, ragged garnet crystal edges and irregular patchy zoning in monazite grains; Figs 2 & 5). All other samples are interpreted to have formed under sub-solidus conditions. The REE partition coefficient profile for LG-09-01 is the closest to the previously-reported values (Fig. 9), suggesting either that the presence of melt may affect garnet–monazite partitioning coefficients or that melt facilitates transport of REE to/from phases that were growing or breaking down. The fact that we did not measure the REE concentrations in monazite inclusions in garnet means that despite the age similarities, there could be chemical differences between the matrix monazite cores and the populations included in garnet. Further detailed work is needed to assess this.

The presence of a free hydrous phase is more difficult to assess in our samples. The presence/absence and amount of grain boundary fluid during any stage of metamorphism would likely have had an effect on the transport efficiency of the REE. The samples reported in the previous studies and those presented here contain hydrous phases such as biotite, suggesting that none of the samples was completely anhydrous. The local availability of fluid could have affected the efficiency of REE transport within the sample, and could thus have affected local equilibration between monazite and garnet. Further detailed studies that investigate the effect of excess or limited water on the mineralogical evolution of samples in any of the four studies would help to resolve whether availability of fluid is a factor in the difference between our dataset and those previously published.

Other co-crystallizing accessory phases such as zircon may compete for available HREE, and apatite may compete for available MREE. Zircon–garnet partition coefficients are near unity for many of the REE, with zircon showing a slight increased preference for the HREE (Rubatto et al. 2001; Taylor et al. 2015). Zircon is likely to have been reactive in the melt-present samples reported in the previous garnet–monazite partitioning studies. Zircon is highly refractory and only tends to crystallize

in metapelites in the presence of melt (e.g. Rubatto et al. 2013). In our samples, the absence of melt suggests that metamorphic zircon was not co-crystallizing with garnet and monazite. Furthermore, low Th/U ratios in monazite compared to previous studies also suggest that zircon was not competing for available U. However, since zircon was neither imaged nor analysed in any of our samples, the lack of involvement of zircon crystallization here remains conjectural.

Similar to our samples, garnet in all previously reported datasets is almandine (Fe)-rich. Garnet in LG-09-01 is $Alm_{0.67}$ whereas all other samples are $Alm_{0.78-0.73}$. The garnet in the samples reported by Hermann & Rubatto (2003) is $Alm_{0.63}$, that by Rubatto et al. (2006) is $Alm_{0.85-0.80}$ and that by Buick et al. (2006) is $Alm_{0.74-0.62}$ (Table 4). The spessartine (Mn) component in all garnets in our and those previous studies (apart from LG-09-01) is uniformly low at <5%. Similarly, the grossular (Ca) component in all sample garnets is uniform and <5%. We therefore do not think that garnet composition plays a major role in the partitioning of HREE between garnet and monazite.

The compositional control of monazite on its REE partitioning behaviour is more difficult to assess. Monazite chemistry can vary widely depending on local bulk composition. The monazites in our samples, which are all pelites of similar bulk composition, show similar behaviour (Figs 5 & 9). However, there is not enough information in the previously reported studies on the composition of monazite to compare and contrast our samples.

Implications for using partitioning patterns to link age to stage

In summary, there are multiple factors that could have influenced the different garnet–monazite relationship patterns that we see in our sample set. On balance, we suggest the most likely reasons for the differences are competition for the REE by other competing phases or subtle variations in monazite chemistry that affect its incorporation of available REEs. We acknowledge that our dataset is only preliminary and that further work is needed to constrain garnet–monazite partitioning relationships more tightly.

Further datasets are needed from a variety of natural samples to fully explore the implications of our findings, especially the mapping of local equilibration volumes in different samples, the effect of metamorphic grade and lithological controls on partitioning behaviour. In the meantime, caution is urged in applying any of the reported garnet–monazite REE trends to 'prove' equilibrium for linking monazite age to metamorphic stage.

Conclusions

Recent analytical developments that allow increasing spatial precision in geochemical analyses have allowed geochronological information recorded in zoned accessory phases to be linked to the PT information recorded in zoned major rock-forming minerals. Previous empirical studies have derived garnet–monazite REE partition coefficients that have subsequently been used to demonstrate an 'age to stage' link via monazite ages and garnet growth stages. We have analysed REE concentrations in zoned monazite and garnet grains from samples of amphibolite-facies felsic gneiss from Bhutan where age and textural and chemical constraints link the growth of monazite to the growth of garnet. We find that relative to previous studies, the garnet–monazite partitioning coefficients for the HREEs are lower, thus creating a steeper partitioning coefficient slope. The difference between our data and data reported in previous studies may be due to a variety of as-yet unconstrained factors including (but not limited to) the presence of another phase competing for the available REE during growth, the temperature-dependence of the partitioning coefficients or variations in monazite chemistry causing different REE partitioning behaviour. Until these issues are resolved, we caution against using empirically derived partition coefficients from natural samples as evidence for, or against, equilibrium of REE-bearing phases. Indeed, consistent partitioning of REEs between garnet and monazite in a suite of samples provides necessary but not sufficient evidence for chemical equilibrium between coexisting monazite and garnet. Further analyses on a variety of natural samples are needed to refine and constrain the natural variability in garnet–monazite partition coefficients.

References

AYRES, M. & HARRIS, N. 1997. REE fractionation and Nd-isotope disequilibrium during crustal anatexis: constraints from Himalayan leucogranites. *Chemical Geology*, **139**, 249–269.

BUICK, I.S., HERMANN, J., WILLIAMS, I.S., GIBSON, R.L. & RUBATTO, D. 2006. A SHRIMP U–Pb and LA-ICP-MS trace element study of the petrogenesis of garnet–cordierite–orthoamphibole gneisses from the Central Zone of the Limpopo Belt, South Africa. *Lithos*, **88**, 150–172.

CARLSON, W.D. 2012. Rates and mechanisms of Y, REE and Cr diffusion in garnet. *American Mineralogist*, **97**, 1598–1618.

CORRIE, S.L. & KOHN, M.J. 2008. Trace-element distributions in silicates during prograde metamorphic reactions: implications for monazite formation. *Journal of Metamorphic Geology*, **26**, 451–464.

CORRIE, S.L., KOHN, M.J., MCQUARRIE, N. & LONG, S.P. 2012. Flattening the Bhutan Himalaya. *Earth and Planetary Science Letters*, **349**, 67–74.

DANIEL, C.G., HOLLISTER, L.S., PARRISH, R.T. & GRUJIC, D. 2003. Exhumation of the Main Central Thrust from lower crustal depths, eastern Bhutan Himalaya. *Journal of Metamorphic Geology*, **21**, 317–334.

FOSTER, G., GIBSON, H.D., PARRISH, R., HORSTWOOD, M., FRASER, J. & TINDLE, A. 2002. Textural, chemical and isotopic insights into the nature and behaviour of metamorphic monazite. *Chemical Geology*, **191**, 183–207.

FROST, B.R. & CHACKO, T. 1989. The granulite uncertainty principle: limitations on thermobarometry in granulites. *The Journal of Geology*, **97**, 435–450.

GREENWOOD, L.V., ARGLES, T.W., PARRISH, R.R., HARRIS, N.B. & WARREN, C. 2016. The geology and tectonics of central Bhutan. *Journal of the Geological Society, London*, **173**, 352–369, https://doi.org/10.1144/jgs2015-031

GRUJIC, D., WARREN, C.J. & WOODEN, J.L. 2011. Rapid synconvergent exhumation of Miocene-aged lower orogenic crust in the eastern Himalaya. *Lithosphere*, **3**, 346–366.

HARRIS, N.B.W., GRAVESTOCK, P. & INGER, S. 1992. Ion-microprobe determinations of trace-element concentrations in garnets from anatectic assemblages. *Chemical Geology*, **100**, 41–49.

HENRY, D.J., GUIDOTTI, C.V. & THOMSON, J.A. 2005. The Ti-saturation surface for low-to-medium pressure metapelitic biotites: implications for geothermometry and Ti-substitution mechanisms. *American Mineralogist*, **90**, 316–328.

HERMANN, J. & RUBATTO, D. 2003. Relating zircon and monazite domains to garnet growth zones: age and duration of granulite facies metamorphism in the Val Malenco lower crust. *Journal of Metamorphic Geology*, **21**, 833–852.

HODGES, K.V. 2000. Tectonics of the Himalaya and southern Tibet from two perspectives. *Geological Society of America Bulletin*, **112**, 324–350.

HOLDAWAY, M.J. 2000. Application of new experimental and garnet Margules data to the garnet–biotite geothermometer. *American Mineralogist*, **85**, 881–892.

HOLLAND, T.J.B. & POWELL, R. 1998. An internally consistent thermodynamic data set for phases of

petrological interest. *Journal of Metamorphic Geology*, **16**, 309–343.

HORSTWOOD, M.S.A., KOŠLER, J. *ET AL.* 2016. Community-derived standards for LA-ICP-MS U-(Th)-Pb geochronology–uncertainty propagation, age interpretation and data reporting. *Geostandards and Geoanalytical Research*, **40**, 311–332.

JANOTS, E., ENGI, M., BERGER, A., ALLAZ, J., SCHWARZ, J.O. & SPANDLER, C. 2008. Prograde metamorphic sequence of REE minerals in pelitic rocks of the Central Alps: implications for allanite–monazite–xenotime phase relations from 250°C to 610°C. *Journal of Metamorphic Geology*, **26**, 509–526.

KELLY, N.M., HARLEY, S.L. & MÖLLER, A. 2012. Complexity in the behavior and recrystallization of monazite during high-T metamorphism and fluid infiltration. *Chemical Geology*, **322**, 192–208.

KOHN, M.J., WIELAND, M.S., PARKINSON, C.D. & UPRETI, B.N. 2005. Five generations of monazite in Langtang gneisses: implications for chronology of the Himalayan metamorphic core. *Journal of Metamorphic Geology*, **23**, 399–406.

KONRAD-SCHMOLKE, M., ZACK, T., O'BRIEN, P.J. & JACOB, D.E. 2008. Combined thermodynamic and rare earth element modelling of garnet growth during subduction: examples from ultrahigh-pressure eclogite of the Western Gneiss Region, Norway. *Earth and Planetary Science Letters*, **272**, 488–498.

LONG, S.P., McQUARRIE, N. *ET AL.* 2012. Variable shortening rates in the eastern Himalayan thrust belt, Bhutan: insights from multiple thermochronologic and geochronologic data sets tied to kinematic reconstructions. *Tectonics*, **31**, https://doi.org/10.1029/2012TC00 3155

LUDWIG, K.R. 2003. *Isoplot 3.00: A Geochronological Toolkit for Microsoft Excel*. Berkeley Geochronology Center Special Publication, 4. Berkeley, CA.

MOTTRAM, C.M., WARREN, C.J., REGIS, D., ROBERTS, N.M., HARRIS, N.B., ARGLES, T.W. & PARRISH, R.R. 2014. Developing an inverted Barrovian sequence; insights from monazite petrochronology. *Earth and Planetary Science Letters*, **403**, 418–431.

MOTTRAM, C.M., PARRISH, R.R., REGIS, D., WARREN, C.J., ARGLES, T.W., HARRIS, N.B. & ROBERTS, N.M. 2015. Using U–Th–Pb petrochronology to determine rates of ductile thrusting: time windows into the Main Central Thrust, Sikkim Himalaya. *Tectonics*, **34**, 1355–1374.

OTAMENDI, J.E., DE LA ROSA, J.D., PATIÑO DOUCE, A.E. & CASTRO, A. 2002. Rayleigh fractionation of heavy rare earths and yttrium during metamorphic garnet growth. *Geology*, **30**, 159–162.

PALIN, R.M., SEARLE, M.P. *ET AL.* 2013. A geochronological and petrological study of anatectic paragneiss and associated granite dykes from the Day Nui Con Voi metamorphic core complex, North Vietnam: constraints on the timing of metamorphism within the Red River shear zone. *Journal of Metamorphic Geology*, **31**, 359–387, https://doi.org/10.1111/jmg.12025

PALME, H. & O'NEILL, H.S.C. 2014. 3.1 - Cosmochemical estimates of mantle composition A2. *In*: HOLLAND, H. &TUREKIAN, E. (eds) *Treatise on Geochemistry*. Elsevier, Oxford, **3**, 1–39, http://www.sciencedirect.com/science/article/pii/B9780080959757002011

PARRISH, R.R. 1990. U–Pb dating of monazite and its application to geological problems. *Canadian Journal of Earth Sciences*, **27**, 1431–1450.

PYLE, J.M. & SPEAR, F.S. 2003. Four generations of accessory-phase growth in low-pressure migmatites from SW New Hampshire. *American Mineralogist*, **88**, 338–351.

REGIS, D., WARREN, C.J., MOTTRAM, C.M. & ROBERTS, N.M.W. 2016. Using monazite and zircon petrochronology to constrain the P–T–t evolution of the middle crust in the Bhutan Himalaya. *Journal of Metamorphic Geology*, **34**, 617–639, https://doi.org/10.1111/jmg.12196

ROWLEY, D.B. 1996. Age of initiation of collision between India and Asia: a review of stratigraphic data. *Earth and Planetary Science Letters*, **145**, 1–13.

RUBATTO, D., WILLIAMS, I.S. & BUICK, I.S. 2001. Zircon and monazite response to prograde metamorphism in the Reynolds Range, central Australia. *Contributions to Mineralogy and Petrology*, **140**, 458–468.

RUBATTO, D., HERMANN, Jör. & BUICK, I.S. 2006. Temperature and bulk composition control on the growth of monazite and zircon during low-pressure anatexis (Mount Stafford, central Australia). *Journal of Petrology*, **47**, 1973–1996.

RUBATTO, D., CHAKRABORTY, S. & DASGUPTA, S. 2013. Timescales of crustal melting in the Higher Himalayan Crystallines (Sikkim, Eastern Himalaya) inferred from trace element-constrained monazite and zircon chronology. *Contributions to Mineralogy and Petrology*, **165**, 349–372.

SEYDOUX-GUILLAUME, A.M., MONTEL, J.M. *ET AL.* 2012. Low-temperature alteration of monazite: fluid mediated coupled dissolution–precipitation, irradiation damage, and disturbance of the U–Pb and Th–Pb chronometers. *Chemical Geology*, **330**, 140–158.

SIMPSON, R.L., PARRISH, R.R., SEARLE, M.P. & WATERS, D.J. 2000. Two episodes of monazite crystallization during metamorphism and crustal melting in the Everest region of the Nepalese Himalaya. *Geology*, **28**, 403–406.

SKORA, S., BAUMGARTNER, L.P., MAHLEN, N.J., JOHNSON, C.M., PILET, S. & HELLEBRAND, E. 2006. Diffusion-limited REE uptake by eclogite garnets and its consequences for Lu–Hf and Sm–Nd geochronology. *Contributions to Mineralogy and Petrology*, **152**, 703–720.

STACEY, J.S. & KRAMERS, J.D. 1975. Approximation of terrestrial lead isotope evolution by a two-stage model. *Earth and Planetary Science Letters*, **26**, 207–221.

SWAPP, S.M. & HOLLISTER, L.S. 1991. Inverted metamorphism within the Tibetan slab of Bhutan; evidence for a tectonically transported heat-source. *The Canadian Mineralogist*, **29**, 1019–1041.

TAYLOR, R.J.M., HARLEY, S.L., HINTON, R.W., ELPHICK, S., CLARK, C. & KELLY, N.M. 2015. Experimental determination of REE partition coefficients between zircon, garnet and melt: a key to understanding high-T crustal processes. *Journal of Metamorphic Geology*, **33**, 231–248.

TOBGAY, T., McQUARRIE, N., LONG, S., KOHN, M.J. & CORRIE, S.L. 2012. The age and rate of displacement along the Main Central Thrust in the western Bhutan Himalaya. *Earth and Planetary Science Letters*, **319**, 146–158.

WARREN, C.J., GRUJIC, D., KELLETT, D.A., COTTLE, J., JAMIESON, R.A. & GHALLEY, K.S. 2011. Probing the depths of the India-Asia collision: U–Th–Pb monazite chronology of granulites from NW Bhutan. *Tectonics*, **30**, https://doi.org/10.1029/2010TC002738

WHITNEY, D.L. & EVANS, B.W. 2010. Abbreviations for names of rock-forming minerals. *American Mineralogist*, **95**, 185.

WOOD, B.J. & BLUNDY, J.D. 1997. A predictive model for rare earth element partitioning between clinopyroxene and anhydrous silicate melt. *Contributions to Mineralogy and Petrology*, **129**, 166–181.

WOODSWORTH, G. 1977. Homogenization of zoned garnets from pelitic schists. *Canadian Mineralogist*, **15**, 230–242.

WU, C.-M. 2015. Revised empirical garnet–biotite–muscovite–plagioclase geobarometer in metapelites. *Journal of Metamorphic Geology*, **33**, 167–176.

WU, C.-M. & CHEN, H.-X. 2015. Revised Ti-in-biotite geothermometer for ilmenite-or rutile-bearing crustal metapelites. *Science Bulletin*, **60**, 116–121.

WU, C.-M. & CHENG, B.-H. 2006. Valid garnet–biotite (GB) geothermometry and garnet–aluminum silicate–plagioclase–quartz (GASP) geobarometry in metapelitic rocks. *Lithos*, **89**, 1–23.

ZEIGER, K., GORDON, S.M., LONG, S.P., KYLANDER-CLARK, A.R.C., AGUSTSSON, K. & PENFOLD, M. 2015. Timing and conditions of metamorphism and melt crystallization in Greater Himalayan rocks, eastern and central Bhutan: insight from U–Pb zircon and monazite geochronology and trace-element analyses. *Contributions to Mineralogy and Petrology*, **169**, 47, https://doi.org/10.1007/s00410-015-1143-6

ZHU, B., KIDD, W.S., ROWLEY, D.B., CURRIE, B.S. & SHAFIQUE, N. 2005. Age of initiation of the India–Asia collision in the east-central Himalaya. *The Journal of Geology*, **113**, 265–285.